



HAL
open science

Ultrasonic monitoring of spontaneous imbibition experiments: Precursory moisture diffusion effects ahead of water front

Christian David, Joël Sarout, Jérémie Dautriat, Lucas Pimienta, Marie Michée, Mathilde Desrues, Christophe Barnes

► To cite this version:

Christian David, Joël Sarout, Jérémie Dautriat, Lucas Pimienta, Marie Michée, et al.. Ultrasonic monitoring of spontaneous imbibition experiments: Precursory moisture diffusion effects ahead of water front. *Journal of Geophysical Research: Solid Earth*, 2017, 122 (7), pp.4948-4962. 10.1002/2017JB014193 . hal-03888091

HAL Id: hal-03888091

<https://hal.science/hal-03888091>

Submitted on 9 Dec 2022

HAL is a multi-disciplinary open access archive for the deposit and dissemination of scientific research documents, whether they are published or not. The documents may come from teaching and research institutions in France or abroad, or from public or private research centers.

L'archive ouverte pluridisciplinaire **HAL**, est destinée au dépôt et à la diffusion de documents scientifiques de niveau recherche, publiés ou non, émanant des établissements d'enseignement et de recherche français ou étrangers, des laboratoires publics ou privés.

Copyright

RESEARCH ARTICLE

10.1002/2017JB014193

Special Section:

Seismic and micro-seismic signature of fluids in rocks: Bridging the scale gap

This article is a companion to David *et al.* [2017] doi:10.1002/2016JB013804.

Key Points:

- *P* waves velocity and amplitude were recorded in imbibition tests on 14 different rock samples
- Moisture diffusion accounts for the precursory *P* wave amplitude drop before the arrival of liquid water in the sensors Fresnel zone
- The time at amplitude drop provides an estimate of the effective moisture diffusivity which is found to correlate with permeability

Correspondence to:

C. David,
christian.david@u-cergy.fr

Citation:

David, C., J. Sarout, J. Dautriat, L. Pimienta, M. Michée, M. Desrues, and C. Barnes (2017), Ultrasonic monitoring of spontaneous imbibition experiments: Precursory moisture diffusion effects ahead of water front, *J. Geophys. Res. Solid Earth*, 122, 4948–4962, doi:10.1002/2017JB014193.

Received 10 MAR 2017

Accepted 24 JUN 2017

Accepted article online 29 JUN 2017

Published online 18 JUL 2017

Ultrasonic monitoring of spontaneous imbibition experiments: Precursory moisture diffusion effects ahead of water front

Christian David¹ , Joël Sarout² , Jérémie Dautriat², Lucas Pimienta³ , Marie Michée², Mathilde Desrues^{1,4}, and Christophe Barnes¹ ¹Laboratoire Géosciences et Environnement Cergy, Université de Cergy-Pontoise, Cergy-Pontoise, France, ²CSIRO Energy, Perth, Western Australia, Australia, ³Laboratoire de Géologie de l'ENS, PSL Research University UMR 8538 du CNRS, Paris, France, ⁴EOST, Université de Strasbourg, Strasbourg, France

Abstract Fluid substitution processes have been investigated in the laboratory on 14 carbonate and siliciclastic reservoir rock analogues through spontaneous imbibition experiments on vertical cylindrical specimens with simultaneous ultrasonic monitoring and imaging. The motivation of our study was to identify the seismic attributes of fluid substitution in reservoir rocks and to link them to physical processes. It is shown that (i) the *P* wave velocity either decreases or increases when the capillary front reaches the Fresnel clearance zone, (ii) the *P* wave amplitude is systematically impacted earlier than the velocity is, (iii) this precursory amplitude decrease occurs when the imbibition front is located outside of the Fresnel zone, and (iv) the relative variation of the *P* wave amplitude is always much larger than that of the *P* wave velocity. These results suggest that moisture diffuses into the pore space ahead of the water front. This postulate is further supported by a quantitative analysis of the time evolution of the observed *P* wave amplitudes. In a sense, *P* wave amplitude acts as a precursor of the arrival of the capillary front. This phenomenon is used to estimate the effective diffusivity of moisture in the tested rocks. The effective moisture diffusivity estimated from the ultrasonic data is strongly correlated with permeability: a power law with exponent 0.96 predicts permeability from ultrasonic monitoring within a factor 3 without noticeable bias. When the effective diffusivity is high, moisture diffusion affects ultrasonic *P* wave attributes even before the imbibition starts and impacts the *P* wave reflectivity as evidenced by the variations recorded in the waveform coda.

1. Introduction

Fluid substitution processes can lead to significant modifications in the physical properties of porous rocks which can impact gas and oil recovery [Doornhof *et al.*, 2006], groundwater management [Novakowski and Gillham, 1988], CO₂ geosequestration operations [JafarGandomi and Curtis, 2011], and geothermal energy extraction [Jaya *et al.*, 2008]. Remote seismic monitoring has been proposed as a tool to characterize fluid substitution processes in underground reservoirs [Rasolofosaon and Zinszner, 2004], as the elastic properties of reservoir rocks are very sensitive to the nature of the fluids saturating the pore space [Mavko *et al.*, 2009; Rasolofosaon and Zinszner, 2012]. Fluid substitution in porous rocks, driven by either natural (e.g., wetting/drying processes) or man-induced (e.g., water flooding in hydrocarbon reservoirs) forces, commonly occurs in nature. One way to address this problem in the laboratory is to perform spontaneous imbibition experiments in which a wetting fluid (e.g., water) replaces a nonwetting phase (e.g., air) originally present in the pore space. Assessing fluid substitution and redistribution processes in underground reservoirs requires the implementation of remote surface geophysical monitoring techniques such as seismic surveys. A laboratory equivalent of a seismic survey is achieved by using an array of ultrasonic transducers (source/receiver pairs) coupled to a rock sample during a simulated fluid substitution experiment under well-controlled conditions. Such a setup can be used during fluid substitution experiments on rock specimens at room conditions (e.g., spontaneous imbibition reported here) or at the in situ stress conditions during forced fluid injection experiments in a triaxial stress vessel [David *et al.*, 2015a]. For a correct interpretation of the seismic signals, it is also necessary to link the variation in seismic attributes (velocity and attenuation) to the actual distribution of fluids in the rock. The feasibility of ultrasonic monitoring in laboratory experiments was assessed in water flooding experiments by Wulff and Mjaaland [2002] and in fluid injection experiments with simultaneous acoustic emissions and ultrasonic monitoring by Stanchits *et al.* [2011]. Ultrasonic monitoring of injection experiments was also recently conducted by Lopes *et al.* [2012, 2014], and the

effect of capillarity on P wave attenuation and dispersion has been studied theoretically by *Qi et al.* [2014]. Our recent works [*David et al.*, 2015a; *Dautriat et al.*, 2016] showed that during water injection into a poorly consolidated sandstone originally saturated with air or oil, the P wave velocity decreases. In sedimentary rocks, the P wave velocity decrease induced by water injection is often referred to as chemical weakening [*Knight and Dvorkin*, 1992; *Mavko et al.*, 2009]. Water vapor has also a significant weakening effect when adsorbed on mineral surfaces and/or at grain contacts. In the laboratory experiments they conducted on a set of sandstones and limestones, *Pimienta et al.* [2014] found that relative humidity impacts significantly seismic attributes (P wave and S wave velocity and amplitude), especially in poorly cemented sandstones. In these experiments the water saturation is lower than few percent, and the weakening is essentially due to moisture diffusion in the pore space. A grain contact theory [*Digby*, 1981], extended to include the effect of surface energy reduction by moisture adsorption, successfully models the experimental observations [*Pimienta et al.*, 2014]. The impact of moisture diffusion on the nonlinear elasticity in porous rocks was studied by *van Den Abeele et al.* [2002].

In addition, for a successful application in the field, the remotely monitored variations in seismic attributes have to be correlated with the actual evolution of the distribution of the fluid within the porous rock during fluid substitution [*Avseth et al.*, 2005]. To this end, imaging techniques are well suited for characterizing the fluid distribution in the pore space. At the laboratory scale, this can be achieved using attenuation maps obtained by exposing the tested rock to X-ray [*Mees et al.*, 2003] or neutron [*Hall*, 2013] beams during the fluid substitution process. In a recent study, *David et al.* [2015b] recorded the P waveforms transmitted between two pairs of ultrasonic transducers (~ 0.5 MHz) located at two heights along vertical rock specimens subjected to spontaneous water imbibition experiments. Simultaneously, X-ray CT images were acquired with a Siemens SOMATOM Definition AS 64-slice. They showed that the P wave amplitude drops systematically before the P wave velocity is impacted by the approaching water front. Furthermore, this amplitude drop occurs when the fluid front appears to be located well below the zone probed by the two ultrasonic source/receiver pairs. A similar behavior was reported in a companion paper of the same special volume [*David et al.*, 2017] on two additional rocks, the Majella grainstone and the Sherwood sandstone. Whereas the relationship between the fluid front position and the onset of velocity decrease could be explained by taking into account the size of the Fresnel clearance zone [*Spetzler and Snieder*, 2004], no clear explanation could be given for the decoupled evolution of P wave amplitude and velocity. The overall conclusion drawn from these results is that the P wave amplitude (related to the P wave attenuation) is more sensitive to fluid substitution processes than the P wave velocity. This conclusion is consistent with that of *Wulff and Mjaaland* [2002]. No physical explanation was given for the early amplitude decrease observed in all the rocks studied so far.

In the present work we postulate that the observed P wave amplitude decrease during spontaneous imbibition experiments is related to moisture (water vapor) diffusion ahead of the water front. To support this postulate, new experimental results are presented, and a unified interpretation is devised for the complete data set, including our recently published results. Our analysis shows that at the laboratory scale, fluid substitution processes can be well detected by remote ultrasonic methods, with amplitude variations being a precursory signal ahead of the arrival of the fluid front. Furthermore, the analysis of amplitude variations provides a robust way to estimate the effective diffusivity of water vapor in porous rocks. For our data set, the effective diffusivity-permeability relationship is a power law, which suggests a convenient and cost-effective method for predicting permeability from ultrasonic measurements during spontaneous imbibition experiments, within a factor 3 uncertainty.

2. Materials and Methods

An experimental protocol was designed for conducting simple fluid substitution experiments, i.e., spontaneous imbibition, with simultaneous ultrasonic monitoring and imaging of the inner structure of the rock. Such experiments have been conducted in Commonwealth Scientific and Industrial Research Organisation's (CSIRO) Geomechanics and Geophysics Laboratory located in Perth (Australia). All experiments were done on unjacketed samples, under room pressure and controlled temperature (25°C). Two pairs of P wave ultrasonic transducers (two source/receiver pairs) are attached to vertical rock samples (length ~ 80 mm) at two different heights (~ 25 and 50 mm). A specific stand is designed to allow water to be in

Table 1. Selected Rocks for the Imbibition Experiments With Imaging and Ultrasonic Monitoring^a

Rock Sample	(S)andstone (C)arbonate	Reference	Porosity (%)	<i>P</i> Wave Velocity of Dry Rock (m/s)	Permeability (mD)
Boise	S	BOI	28.9	2770	3403
Bentheimer	S	BEN	24.4	2780	2370
Saint-Maximin ^b	C	SMX	37.0	2740	2100
Castlegate	S	CSG	25.1	1660	1193
Majella ^c	C	MAJ	30.0	2100	450
Sherwood vertical	S	SH-ver	30.0	1800	350
Leopard	S	LEO	21.1	2570	347
Sherwood horizontal ^c	S	SH-hor	30.0	1400	200
Silurian dolomite	C	SID	14.3	5240	199
Berea	S	BER	18.6	2240	107
Carbon Tan	C	CAT	16.6	2160	55.2
Edward Brown	C	EDB	25.9	3560	30.8
Savonnières	C	SAV	32.2	3160	28.2
Tuffeau	C	TUF	38.9	1920	25.6

^aBoth permeability and *P* wave velocity are measured along the sample axis. The sample list is ordered with respect to permeability, from the most permeable to the least permeable sample.

^bDavid et al. [2015b].

^cDavid et al. [2017].

contact with the bottom end of the rock specimen, allowing a spontaneous water imbibition process to occur [David et al., 2015b]. In addition, this arrangement allows for a time-lapse imaging of the water distribution within the rock specimen using, for instance, X-ray CT monitoring. These images represent density maps of the inside of the rock sample taken every 5 s during the imbibition process. The same time-lapse interval is used for the ultrasonic *P* wave monitoring: every 5 s the waveform transmitted between each of the two pairs of source/receiver is recorded, and the *P* wave velocity and amplitude are calculated. The first results of this kind of experiments on four rock samples were published by David et al. [2015b, 2017]. Here we present unpublished results which allow us to extend our data set to 14 different rock samples that experienced similar spontaneous imbibition tests with imaging and ultrasonic monitoring (Table 1). Seven carbonate rocks and six sandstones were selected in order to cover a wide range of porosity and permeability relevant for reservoir analogues. Two orthogonal samples of Sherwood sandstone were tested to assess the effect of anisotropy. The so-called vertical specimen (SH-ver) is cored parallel to the bedding plane so that the bedding appears vertical. The opposite holds for the horizontal specimen (SH-hor). Table 1 summarizes the properties of our sample set, listed in decreasing order of permeability.

Note that the results for SMX, MAJ, and SH-hor have been published in David et al. [2015b, 2017]; the others are unpublished results. This sample set covers a porosity range between 14% and 39% and a permeability range between 26 mD and 3400 mD. The permeability data were obtained using the steady state flow method at low confining pressure.

3. Results From Spontaneous Imbibition Tests

3.1. Result for the “Vertical” Sherwood Sandstone

As the sample set is large, it is unpractical to present extensively our observations for all the samples. We therefore report all measurements in Appendix A and present and discuss in detail the results for one representative example: SH-ver the vertical Sherwood sandstone (Figure 1). This experiment was done on a sample cored from the same block as the SH-hor sample studied by David et al. [2017] but in a direction parallel to bedding. Therefore, on CT images the bedding appears to be vertical. Comparing the results for SH-hor and SH-ver allows us to discuss the impact of anisotropy in our experiments.

In Figure 1a, the height of the water front imaged by X-ray CT is plotted as a function of the square root of time clearly: this figure clearly illustrates the anisotropic nature of the Sherwood sandstone. The kinetics of water imbibition in the vertical specimen of Sherwood sandstone (SH-ver) is significantly faster than in the horizontal specimen (SH-hor). Note that at the beginning both plots look similar; then they diverge after water has reached a height of about 10 mm. This contrast in kinetics is in good agreement with the

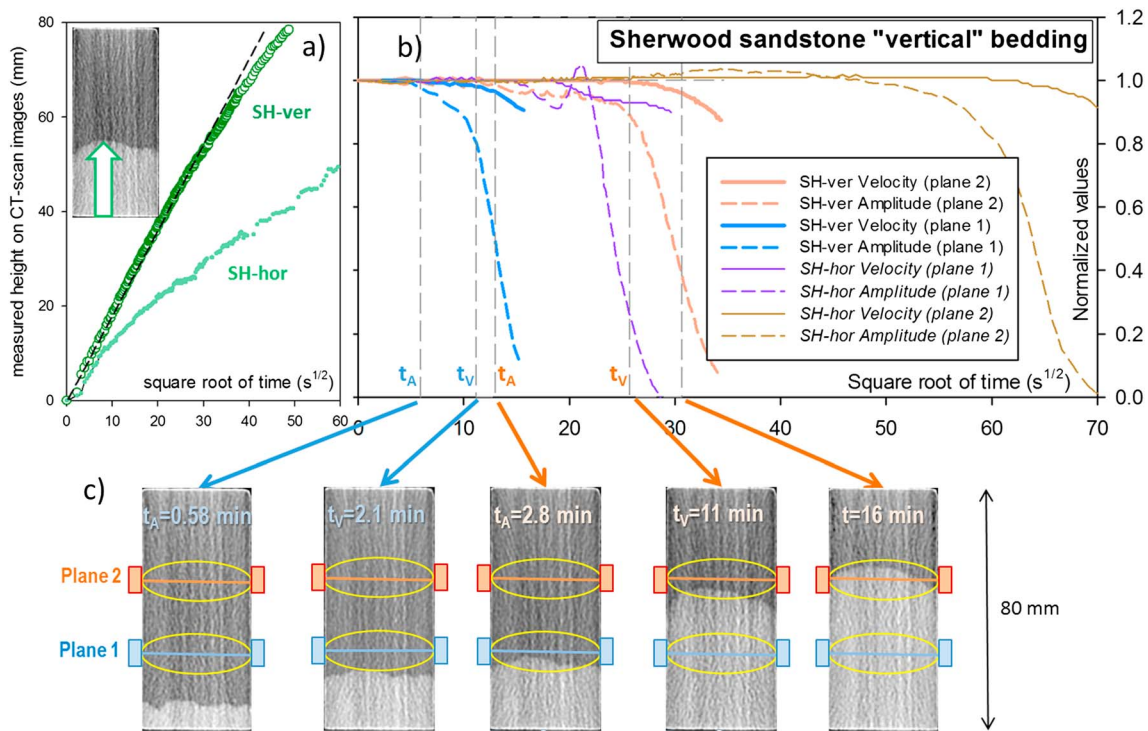


Figure 1. Imbibition experiment with ultrasonic monitoring and X-ray CT scan for the vertical Sherwood sandstone sample SH-ver with bedding parallel to the core axis. (a) Evolution of the water front height measured on the images versus square root of time; for comparison the height evolution for the “horizontal” Sherwood sandstone sample SH-hor is also plotted. (b) Evolution of *P* wave amplitude and velocity (normalized to their value when imbibition starts) versus time (thick blue and orange lines). For comparison the results for the SH-hor samples are shown as well (thin purple and brown lines). (c) Selected CT-scan images during the imbibition process in SH-ver. The ellipses centered on the transducers planes represent the Fresnel clearance zone.

permeability contrast between both samples (Table 1). This is an expected result: permeability along the bedding is almost always larger than across the bedding in sedimentary rocks. Figure 1b shows the evolution during the imbibition process of seismic attributes (velocity and amplitude), derived from the analysis of the waveforms recorded by each pair of ultrasonic transducers located on planes 1 and 2 (more details on data processing are given in David *et al.* [2015b]). X-ray CT images are shown in Figure 1c at five selected times: t_A , when the first peak amplitude starts to decrease (images 1 and 3), and t_V , when the *P* wave velocity starts to decrease (images 2 and 4). The last image presented (image 5) corresponds to the time at which the velocity drop is the sharpest in plane 2. From this experiment and the others already published, very reproducible observations can be made on the evolution of seismic attributes:

1. The *P* wave amplitude is systematically affected by the approaching fluid front before the velocity is.
2. The water front at time t_A is located well below the corresponding ultrasonic transducers' plane.
3. The *P* wave velocity is affected at time t_V when the water front appears to be located within the Fresnel clearance zone of the corresponding ultrasonic transducers' plane. The Fresnel clearance zone is an ellipsoidal region (see the ellipses drawn in Figure 1c) centered along a line joining the centers of the source and receiver transducers. It is the zone in which *P* wave propagation is affected by heterogeneities present in this volume [Spetzler and Snieder, 2004].
4. The relative variation of the *P* wave amplitude is systematically and significantly greater than that of the *P* wave velocity.

In the following section, we will show that all these observations were consistently confirmed, with very few exceptions, on the extended data set. Concerning the influence of anisotropy, the velocity and amplitude variations for sample SH-hor [David *et al.*, 2017] are plotted in Figure 1b for comparison. Both amplitude and velocity drops in sample SH-ver occur much sooner compared to sample SH-hor, consistently with the fastest imbibition kinetics in the former sample.

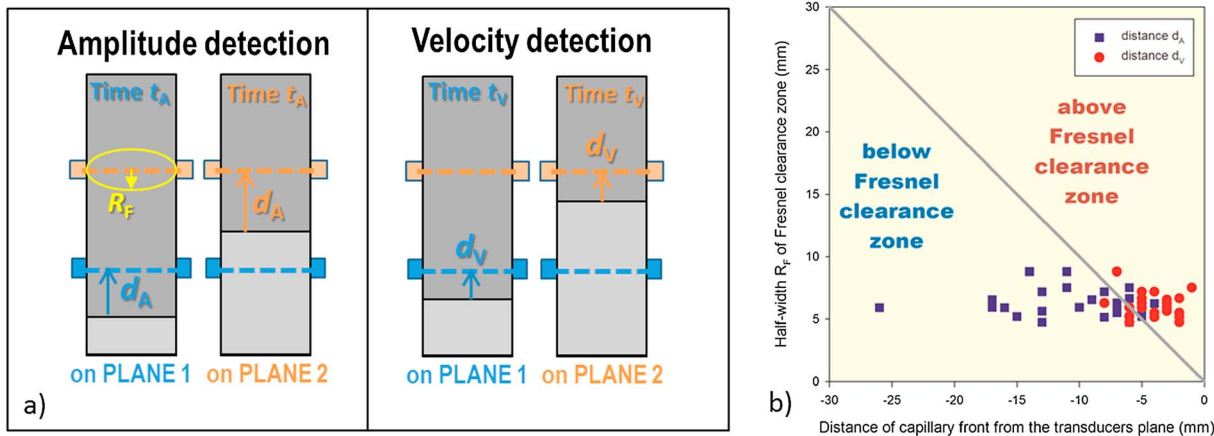


Figure 2. (a) Schematics defining the parameters t_A , d_A , t_V , and d_V listed in Table 2. (b) Crossplot of parameters d_A and d_V versus R_F for all the measurements made on our sample set.

3.2. Results for the Complete Data Set

For sake of completeness, the P wave amplitude and velocity evolutions for the new samples are provided in Appendix A. Note that some curves are noisy: this is due to the fast acquisition rate of ultrasonic waveforms in these experiments, which did not allow for sufficient waveform stacking to improve the signal-to-noise ratio. We will focus here on the analysis of this new data set following the same procedure as for the Sherwood sandstone detailed in the previous section.

Figure 2a shows how the distance d_A (respectively d_V) is defined, between the highest position of the water front and plane 1 or plane 2 at time t_A (respectively t_V) when the seismic attributes depart from their initial value. The half-width R_F of the Fresnel clearance zone (Figure 2a) is calculated using the following relation:

$$R_F = 0.5 \sqrt{\lambda D + \frac{\lambda^2}{4}} \quad (1)$$

where D is the distance between the ultrasonic sensors and λ is the wavelength estimated by the ratio between the P wave velocity and the resonance frequency of the transducers (0.5 MHz). The numerical values for these parameters are given for all the tested samples in Table 2. For both P wave amplitude and velocity, we indicate for “plane 1/plane 2” if the property is decreasing (D) or increasing (I), the time (t_A or t_V) when the property departs from the initial value, the distance (d_A or d_V) of the water front at time t_A or t_V , and the Fresnel zone half-width R_F .

Negative distances correspond to a water front located below the transducers’ plane. Time $t = 0$ corresponds to the time of contact between water and the bottom end of the rock sample. The general conclusions drawn from this analysis on all rock specimens are as follows:

1. The P wave amplitude systematically drops, whether the P wave velocity increases or decreases (except for SID where a slight and temporary increase is observed prior to a significant decrease).
2. The P wave velocity increases, decreases, or remains almost constant depending on the rock tested.
3. The P wave amplitude drop occurs systematically before the P wave velocity varies (except for BEN where it is quasi simultaneous).
4. At time t_V the water front is located within the Fresnel clearance zone.
5. In general, at time t_A the water front is located below the Fresnel clearance zone.
6. The time difference $\Delta t = t_V - t_A$ tends to be larger for rocks with lower permeability.

In Figure 2b, parameters d_A and d_V are plotted versus R_F : with very few exceptions this plot confirms that the P wave amplitude is impacted when the capillary front is below the Fresnel clearance zone, whereas it is located above the Fresnel clearance zone when velocity is impacted. Therefore, our former observations derived from ultrasonic monitoring of imbibition experiments on a limited number of samples

Table 2. Seismic Attributes at the Onset of *P* Wave Amplitude and Velocity Variations During the Imbibition Process^a

Sample	Amplitude Variation (D)decrease (I)increase	Time t_A at Amplitude Variation (s)	Distance d_A From Sensors (mm)	Velocity Variation (D)decrease (I)increase	Time t_V at Velocity Variation (s)	Distance d_V From Sensors (mm)	Half-Width of Fresnel Zone (mm)	Group
BOI	D/D	14/80	-4/-7	I/I	29/96	+6/-3	6.2	blue
BEN	D/D	15/96	-7/-5	I/I	16/95	-8/-5	6.3	
SMX	D/D	55/160	-11/-6	D/D	75/180	-1/-1	7.5	green
CSG	D/D	60/335	-6/-13	D/D	89/499	-2/-6	4.7	
MAJ	D/D	65/390	-9/-17	D/D	165/695	-3/-3	6.6	
SH-ver	D/D	35/170	-16/-26	D/D	125/662	-6/-5	5.9	
LEO	D/D	178/2718	-10/-17	D/D	614/4968	-3/-6	5.9	
SH-hor	D/D	235/1802	-5/-15	D/D	345/3962	-6/-6	5.2	
SID	I, D/I, D	182/2051	-11/-14	I/I	353/2582	-7/-7	8.8	
BER	D/D	1005/7015	-7/-13	D, I/D, I	1411/11494	-3/-3	5.7	red
CAT	D/D	984/4892	-5/-7	I/I	1066/6233	-4/-2	5.5	
EDB	D/D	1660/13797	-8/-13	D, I/D, I	2735/20822	-4/-5	7.2	
SAV	D, I/D	1452/9073	-6/-6	D, I/D, I	2161/9812	-2/-5	6.7	
TUF	D/D	1085/5977	-6/-8	D/D	1354/7589	-4/-2	5.2	

^aThe groups in the last column correspond to different behaviors as explained in section 4.1. Slash symbols separate the properties obtained from analyses on plane 1 and plane 2, respectively.

[David *et al.*, 2015a, 2017] are confirmed with this extended data set including 14 different carbonate and sandstone samples.

4. Discussion: The Impact of Moisture Diffusion

Our extended data set confirms, on a larger number of sandstones and carbonates, that the *P* wave amplitude is systematically impacted before the velocity is during capillary imbibition experiments. Concomitant imaging of the sample's inner structure reveals that this early amplitude variation occurs when the water front is well below the zone probed by the ultrasonic transducers. The evolution of *P* wave velocity (either increase or decrease) is consistent with a water front located close to or above the Fresnel clearance zone [Spetzler and Snieder, 2004]: whether a velocity decrease or increase occurs depends on the competition between bulk moduli and density increase during fluid substitution [Mavko *et al.*, 2009]. *P* wave velocity is strongly dependent on water saturation [Le Ravalec *et al.*, 1996] which was shown to vary with the fluid injection rate [Lopes *et al.*, 2014]: for spontaneous imbibition experiments the fluid injection rate is driven by the magnitude of capillary forces which depends on the rock microstructure. A thorough analysis of CT images after calibration can provide an estimate of the saturation profile in the rock samples [Lopes *et al.*, 2013], which can be linked to the observed velocity variations (work in progress). In contrast, the time of occurrence of the *P* wave amplitude drop requires additional investigation. In the following we examine the experimental evidences supporting the postulate that moisture diffusion is likely the key to understand this puzzling observation.

4.1. Evidence of the Impact of Moisture Diffusion on *P* Wave Amplitude

Water vapor is present in the air as a result of evaporation which takes place, for example, at the surface of a water tank. The amount of water vapor present in the atmosphere depends on the ambient conditions (atmospheric pressure and temperature) and can be related to the relative humidity (RH) parameter. Moisture diffusion in the air is a well-known phenomenon that can be quantified by D_o , the diffusivity of water vapor in the air, equal to $2.82 \cdot 10^{-5} \text{ m}^2/\text{s}$ at 25°C and atmospheric pressure [Cussler, 1997]. For moisture diffusion in a porous medium, an effective diffusivity needs to be defined because of the presence of obstacles (the solid phase) to diffusion [Perkins and Johnston, 1963; Weissberg, 1963]. A general definition for the effective diffusivity in porous media can be found, for example, in van Brakel and Heertjes [1974]:

$$D_{\text{eff}} = \frac{\phi \delta}{\tau^2} D_o \quad (2)$$

where ϕ is the porosity, τ^2 is the tortuosity, and δ is the constrictivity. In this equation, both the tortuosity (related to the increased diffusion path due to obstacles, $\tau^2 \geq 1$) and the constrictivity (related to the pore

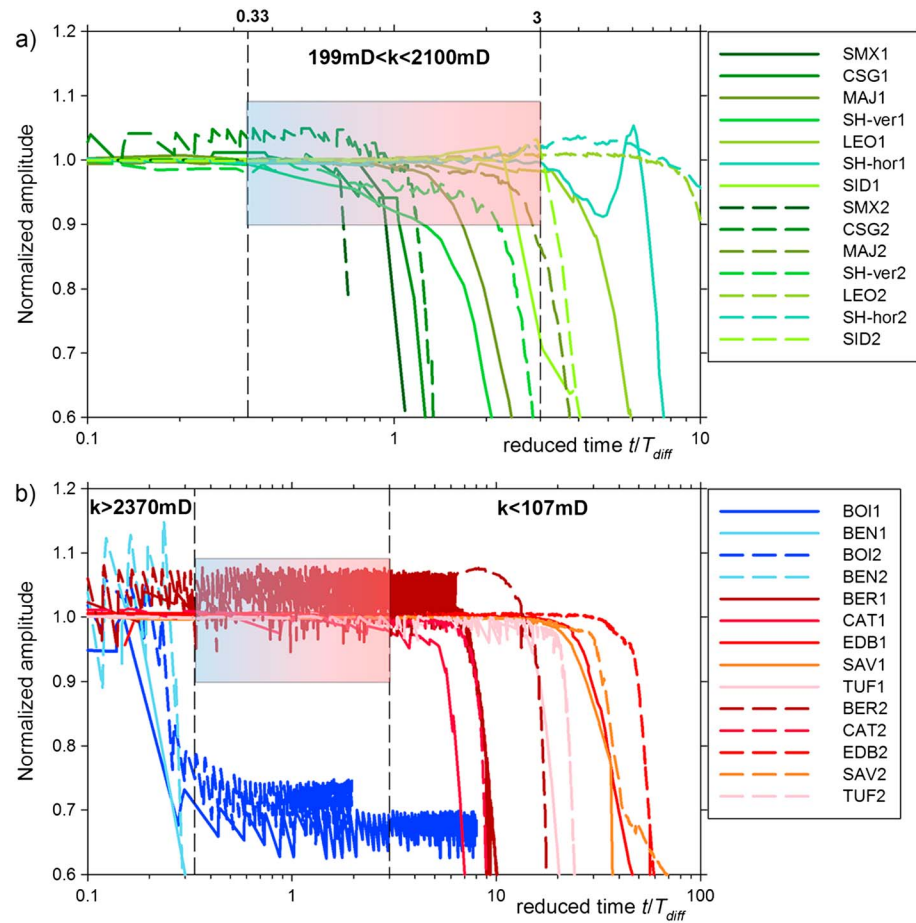


Figure 3. Variation of *P* wave amplitude as a function of the reduced time t/T_{diff} estimated from the vapor diffusion time to reach the sensors planes. (a) Green group, samples with permeability between 199 and 2100 mD, (b) blue group, samples with permeability higher than 2370 mD, and red group, samples with permeability lower than 107 mD. Numbers after sample acronym refer to plane 1 or plane 2.

size variability, $\delta \leq 1$) are unknown and cannot be measured directly. As D_{eff} scales with porosity times intrinsic diffusivity in air, let us define a reduced diffusivity D^* , which can be estimated from the porosity alone:

$$D^* = \phi D_o \tag{3}$$

Then $D_{eff} = \alpha D^*$, where $\alpha = \delta/\tau^2$ is an unknown coefficient. Our postulate is that the early *P* wave amplitude variation occurs when the moisture diffusing in the sample pore space reaches the zone probed by the ultrasonic transducers, first, near plane 1 then near plane 2. As we know the distance *L* between each plane and the bottom end of the sample where moisture diffusion starts once contact is established between sample and water, we can estimate the diffusion time from

$$T_{diff} = \frac{L^2}{D^*} \tag{4}$$

This diffusion time is expected to be different for each rock and for each pair of transducers. Then we can normalize the time scale for each experiment by dividing it by the corresponding diffusion time T_{diff} and plot the *P* wave amplitude data set for all the samples on a single plot as a function of the dimensionless “reduced” time t/T_{diff} (Figure 3). Doing so, it is possible to group all the samples into three subsets: the “green,” the “red,” and the “blue” groups (Table 2), which are well defined in terms of permeability range.

1. The green group includes all the samples with permeability between 199 and 2100 mD. For this group, Figure 3a shows that in 12 cases out of 14, the decrease of *P* wave amplitude occurs within a narrow

reduced time interval between approximately 0.33 and 3. This data clustering when time is normalized by diffusion time supports our postulate; i.e., water vapor diffusion is a good candidate for explaining the wave amplitude decrease, given reasonable experimental uncertainties. As the diffusivity used in the calculation was D^* , this subset of data is consistent with an effective diffusivity D_{eff} such that α ranges between 0.33 and 3. Note that most of the curves are clustered at reduced time larger than 1, corresponding to $\alpha < 1$. This is in good agreement with the dependence of α with tortuosity and constrictivity (equation (1)). One outlier is the horizontal Sherwood sandstone—plane 2 (SH-hor2): the reason for this behavior is attributed to the heterogeneity induced by the layering [David *et al.*, 2017] which could explain (i) the nonlinear and irregular rise of liquid water in the specimen during spontaneous water imbibition (Figure 1a) and (ii) the transient amplitude increase in plane 1 at early stages (SH-hor1 in Figures 1b and 3a). The denser layers probably slow down the overall upward migration of liquid water as well as moisture diffusion due to lower local permeability and/or larger tortuosity of the pore space in these layers.

2. The red group includes all the samples with permeability lower than 107 mD. Figure 3b shows that for these samples the amplitude curves cluster at much higher reduced times, which means that the effective diffusivity is strongly reduced. Here α is much smaller and tortuosity is significantly larger according to equation (1). As the samples in this group are those with the lower permeability, this is in good agreement with the permeability dependence on tortuosity in the equivalent channel model [Walsh and Brace, 1984].
3. The blue group is composed of two rock samples exhibiting the highest permeability: the Boise and Bentheimer sandstones. The P wave amplitude decrease occurs at very early stage of the imbibition (small reduced time, Figure 3b). For this group, the data compiled in Table 2 show that the amplitude and the velocity decrease almost simultaneously. A possible explanation of this discrepancy could be that the kinetics of capillary rise in the samples BOI and BEN is very fast, most likely faster than the kinetics of moisture diffusion. Therefore, the analysis of this subset of samples in terms of effective moisture diffusion is not relevant and leads to effective moisture diffusivity values larger than the free moisture diffusivity in air. Further evidence of the effect of moisture diffusion on the seismic attributes of the tested rocks was found at the very early stages of the imbibition experiments, well before liquid water is in contact with the rock samples. These results are reported in Appendix B.

4.2. Effective Moisture Diffusivity From Ultrasonic Data

The observed data clustering when time is normalized by the diffusion time supports our postulate: moisture diffusion is responsible for the precursory P wave amplitude drop when the front of liquid water is still far from the zone probed by the ultrasonic transducers. Assuming that this postulate is correct and pushing the rationale developed so far one step further, the effective moisture diffusivity within the porous rock can be estimated for each rock. Indeed, knowing the location of the transducers' plane (distance L from the bottom end), and the time of occurrence of the amplitude drop t_A (Table 2), the effective moisture diffusivity is given by

$$D_{\text{eff}} = \frac{L^2}{t_A} \quad (5)$$

This equation gives a first-order estimate for the effective diffusivity, assuming that the distance L from the bottom end to the transducers plane is the correct length scale for the diffusion processes; doing so, we neglect the possible impact of the Fresnel zone. Another underlying assumption is that moisture diffusion processes are faster than capillary processes (not true for the blue group), so that we can neglect the additional contribution of the moving capillary front pushing the water vapor cloud upward. Finally, we also neglect the complications that arise from the open boundary conditions (unjacketed samples) which allow part of the moisture to escape from the sample and also the potential impact of the vibrations induced by the transducers on vapor diffusivity. Given these limitations, as the measurements of L and t_A for each plane 1 and plane 2 are available, equation (4) provides two independent estimates of the effective moisture diffusivity for each rock sample. The results for the green and red groups are given in Table 3. As expected, the effective diffusivity values are lower than the free moisture diffusivity in air D_o . Several models have been suggested in the literature to relate the effective moisture diffusivity in porous media to microstructural or bulk parameters like tortuosity and porosity (for a review of such models, see Shen and Chen [2007]). For the sake

Table 3. Values of the Effective Diffusion Coefficient Estimated From the *P* Wave Amplitude Analysis on Each Sensors Plane, From Which Average Diffusivity and Tortuosity Are Derived for Each Sample^a

	Effective Diffusivity $D_{\text{eff}}\text{—Plane 1}$ (m ² /s)	Effective Diffusivity $D_{\text{eff}}\text{—Plane 2}$ (m ² /s)	Average D_{eff}/D_o	Average Tortuosity t^2	Average $\Delta\lambda/\Delta x$	Predicted Permeability (mD)	Predicted/ Measured Permeability
<i>Green Group</i>							
SMX	1.14E−05	1.56E−05	0.4785	0.77	0.88	928	0.44
CSG	1.37E−05	1.04E−05	0.4270	0.59	0.77	831	0.70
MAJ	9.62E−06	6.41E−06	0.2841	1.06	1.03	562	1.25
SH-ver	1.79E−05	1.47E−05	0.5774	0.52	0.72	1111	3.17
LEO	4.50E−06	1.21E−06	0.1012	2.09	1.44	209	0.60
SH-hor	2.66E−06	1.39E−06	0.0718	4.18	2.04	150	0.75
SID	5.18E−06	1.73E−06	0.1224	1.17	1.08	251	1.26
<i>Red Group</i>							
BER	8.84E−07	5.05E−07	0.0246	7.57	2.75	54	0.50
CAT	8.96E−07	6.95E−07	0.0282	5.88	2.43	61	1.11
EDB	5.39E−07	2.54E−07	0.0141	18.43	4.29	31	1.02
SAV	5.28E−07	3.23E−07	0.0151	21.34	4.62	34	1.19
TUF	7.80E−07	5.71E−07	0.0240	16.24	4.03	52	2.04

^aThe correlation between the effective diffusion coefficient and the permeability (Figure 4) allows one to predict permeability values from effective diffusivity.

of simplicity we use equation (2) and calculate the tortuosity from D_{eff} and ϕ , assuming the unknown constrictivity $\delta = 1$. We also estimate the increased diffusion path length $\Delta\lambda/\Delta x$ as the square root of tortuosity [Ghanbarian *et al.*, 2013].

1. Overall, samples in the green group have a relatively large effective diffusivity and low tortuosity, with one noticeable exception. The horizontal Sherwood sandstone, as noted earlier, has a peculiar behavior in this respect, attributed to its layered structure. The most permeable samples exhibit values of the pore network tortuosity lower than 1, which is theoretically unrealizable [Ghanbarian *et al.*, 2013]. This suggests a breakdown of equation (1) for these particularly permeable rocks with very low tortuosity (nearing 1). Presumably, porosity becomes the key controlling parameter in this case as suggested in Shen and Chen [2007].
2. Samples in the red group have a relatively small effective diffusivity and large tortuosity. Tortuosity ranges between 5 and 29, leading to an increased diffusion path length between 2.2 and 5.4, which seems to be a reasonable range [Ghanbarian *et al.*, 2013].

4.3. Permeability From Effective Moisture Diffusivity

Figure 4 represents in a log-log plot the measured permeability against the effective moisture diffusivity normalized by D_o as derived from ultrasonic data (Table 3) for the 12 rocks studied here (i.e., green and red groups). The effective diffusivity values are the average of the values derived from analyses on plane 1 and plane 2. The permeability appears to correlate reasonably well with the effective moisture diffusivity. The uncertainty in the estimation of the effective moisture diffusivity is represented by horizontal error bars in Figure 4 and corresponds to the standard deviation of the values obtained on planes 1 and 2.

Permeability is therefore a power function of effective moisture. This empirical law holds over 2 orders of magnitude in terms of both permeability and effective moisture diffusivity (Figure 4). Using SI units for permeability (m²) and diffusivity (m²/s), we find that

$$k = 4.39 \cdot 10^{-8} (D_{\text{eff}})^{0.96} \tag{6}$$

A similar result was obtained by Boving and Grathwohl [2001] for the diffusion of tracers in sedimentary rocks, although the exponent was higher (1.8 instead of 0.96). Equation (6) can be used to predict permeability from effective moisture diffusivity. The predicted permeability values (Table 3) agree within approximately a factor 3 with the measured permeability. The predicted-over-measured permeability values range between 0.44 and 3.17, with an average of 1.17 and median 1.07. In the worst cases, permeability is either

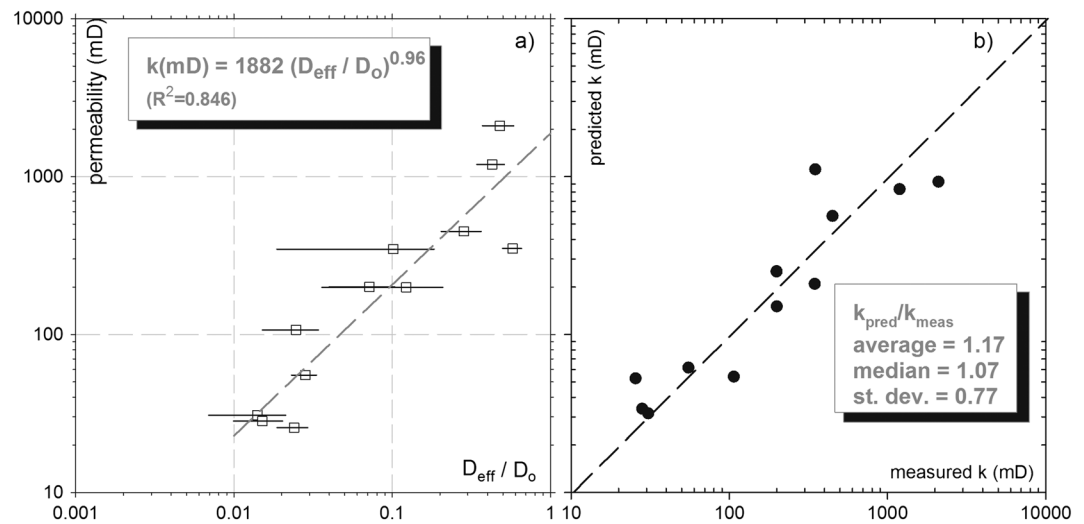


Figure 4. (a) Experimental correlation between the effective diffusivity normalized to water vapor diffusivity in air and permeability for the green and red groups. The horizontal error bars are obtained from the standard deviation of values derived for planes 1 and 2. (b) Predicted versus measured permeability with statistical attributes for the permeability ratio k_{pred}/k_{meas} . (vertical and horizontal scales are identical, and the dashed line corresponds to $k_{pred} = k_{meas}$).

underestimated by a factor ~ 2 or overestimated by a factor ~ 3 at most with little bias, which can be considered as satisfactory regarding permeability prediction in reservoir rocks. The scatter in the data could be related to the uncertainty in defining the time at which moisture diffusion starts (taken here when water contacts the bottom of the sample): our results in Appendix B show that in some samples moisture diffusion can sometimes start before the beginning of capillary rise. Interestingly, a nearly linear relationship between permeability and effective diffusivity is in agreement with the theory of critical path analysis (CPA) [Katz and Thompson, 1986; David et al., 1990], taking into account that diffusivity scales as electrical conductivity: the scatter in the data observed in Figure 4 may be explained by variations of the critical pore radius (the characteristic length scale for permeability according to the CPA theory), which is neglected in our analysis.

In summary, the analysis of the results obtained on 14 different rock samples suggests that the precursory drop in P wave amplitude can be attributed to a faster diffusion of moisture (water vapor) ahead of the front of liquid water. Moisture adsorption on the surface of the minerals was shown to weaken rocks [Clark et al., 1980; Pimienta et al., 2014], leading to a drop in the amplitude of the probing ultrasonic waves before the liquid water visible in the images reaches the Fresnel zone. The arrival of liquid water in the Fresnel clearance zone subsequently induces significant changes in velocity, either decreasing or increasing, depending on the rock. Theoretically, vapor adsorption on mineral grains within the pore space is known to lower the surface energy and therefore the elastic moduli and wave velocities [Johnson et al., 1971; Murphy et al., 1984; Pimienta et al., 2014] as a result of moisture-induced microforces like molecular attraction-repulsion forces [van Den Abeele et al., 2002]. Experimentally, the decrease of both wave velocities and amplitudes was observed from moisture adsorption [Clark et al., 1980; Pimienta et al., 2014] at low water saturation where capillary and swelling microforces are negligible [van Den Abeele et al., 2002]. Here all the tested sandstones and carbonates present elastic weakening by moisture adsorption. Comparatively to these earlier studies, our results suggest that water adsorption on mineral grains has a stronger impact on wave amplitude than it has on wave velocity.

5. Conclusions

A series of spontaneous imbibition experiments were conducted on 14 different rocks with simultaneous ultrasonic monitoring using two pairs of ultrasonic P wave sensors located at different heights. Imaging the fluid substitution process was possible through the acquisition of density maps, which conveniently allowed us to relate the evolution of seismic attributes (P wave amplitude and velocity) to the distribution

of fluids in the pore space. The analysis of the evolution of P waves attributes during the imbibition shows that (i) the P wave velocity is systematically impacted when the capillary front reaches the Fresnel clearance zone associated with the probing ultrasonic transducers, (ii) the P wave amplitude is systematically impacted before velocity is, and (iii) this early amplitude drop occurs when liquid water appears to be located well below the Fresnel clearance zone. When plotting the P wave amplitude evolution as a function of the time scaled by a characteristic diffusion time, the data for both ultrasonic monitoring planes on 14 different rock samples conveniently cluster into three groups depending on the permeability. Precursory moisture diffusion ahead of the front of liquid water is a simple mechanism accounting well for the experimental observations reported here. To our knowledge, this phenomenon has not been previously documented in the geoscience literature. Amplitude drop induced by moisture diffusion can be considered as a precursory signal for the arrival of the capillary front (liquid water). Furthermore, this phenomenon can be used to estimate the effective diffusivity of moisture in rocks, a physical property which depends on the free diffusivity of moisture in the air, the rock porosity, and the tortuosity and constrictivity of the pore network. The effective moisture diffusivity derived from ultrasonic data correlates well with permeability in a range spanning 2 orders of magnitude. This empirical correlation is therefore used to predict permeability from P waves amplitude measurements. For this data set a power law with exponent 0.94 was found, and the ratio of predicted to measured permeability ranges between 0.4 and 3 with a median value close to 1. This uncertainty range is reasonable in view of the notorious variability in permeability usually reported for rocks. For rocks with high effective diffusivity, moisture affects the rock properties at the very early stages of the imbibition experiment, i.e., before liquid water is in contact with the rock. This behavior is attributed to moisture diffusion in the air gap between the sample and the rising water level. Subsequent moisture diffusion near the bottom end of the rock specimens is detected through the changes recorded in the coda of the waveform. Although precursory moisture diffusion has been evidenced in spontaneous imbibition experiments, it is likely to also be acting during forced fluid substitution experiments under triaxial stress states in which precursory P wave amplitude drops have been observed [Dautriat *et al.*, 2016]. Such a diffusion-driven mechanism is likely to occur as well during fluid substitution operations at reservoir scale (e.g., enhanced oil recovery). This study suggests that continuous seismic monitoring involving P wave amplitude analysis is suitable for the early detection and characterization of the distribution of the water injected underground.

Appendix A

The evolution of the normalized P wave velocity and amplitude with time during spontaneous imbibition experiments is presented in Figure A1 for the complete sample set (except for already published data). The results for samples SH-hor, SH-ver, SMX, and MAJ have already been presented in published work [David *et al.*, 2015a, 2017]. The name of the tested rock appears in the same color as the group to which it belongs (blue, green, or red; see section 4).

Appendix B

Moisture diffusion within the rock porous matrix was suspected to occur even before the liquid water rising in the tank had contacted the bottom end of the rock sample. Ultrasonic data and images were recorded during this early stage of the imbibition experiments. These ultrasonic data were analyzed using the methodology developed by David *et al.* [2017], which is briefly recalled here. Each recorded waveform is separated into different wavelets corresponding to different P wave travel paths within the sample (direct wave and reflections). The late wavelet arrivals recorded in the coda correspond to reflections at the bottom end of the sample potentially affected by the diffusing moisture. For the sake of simplicity these late wavelets are referred to as "coda." Figure B1 shows for a selection of rock samples the evolution with time of the energy carried by the coda, normalized by its initial value. This energy is calculated as the time integral of the squared amplitude. At $t = 0$ liquid water in the tank contacts the bottom end of the rock sample. At this time, the energy carried by the coda drops sharply for all the samples. Before the contact ($t < 0$) this energy is constant in all samples but BOI, BEN (blue

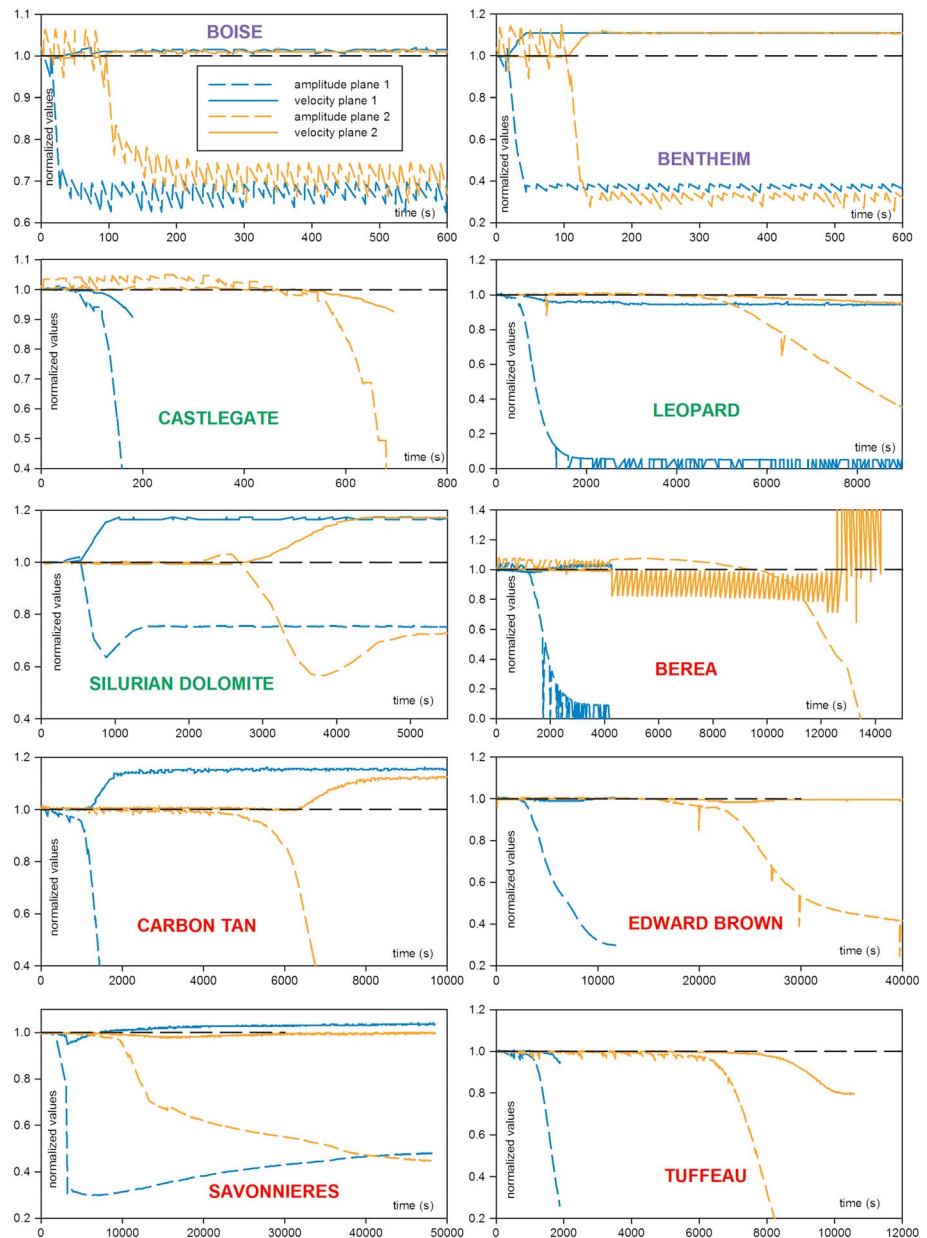


Figure A1. Evolution of normalized *P* wave amplitude and velocity for the extended sample set.

group), and MAJ (green group). For these samples the energy carried by the coda starts decreasing before the rock-water contact.

Let us consider the case of MAJ in more detail because the precursory drop of the energy carried by the *P* wave coda before the contact with liquid water is most pronounced. Figure B2 shows the coda waveforms recorded on plane 1 at five consecutive time steps before and at the time of contact. For each time step, the waveform color corresponds to the color of the X-ray image insert.

Figure B2 clearly shows that the waveform's coda is continuously changing while liquid water has not yet reached the bottom end of the rock sample. This additional observation suggests that moisture diffuses first in the air gap between the rising water front and the bottom end of the sample then within the lower part of the rock sample so that the waveform coda (reflection) recorded at the location of the ultrasonic transducers in plane 1 is impacted.

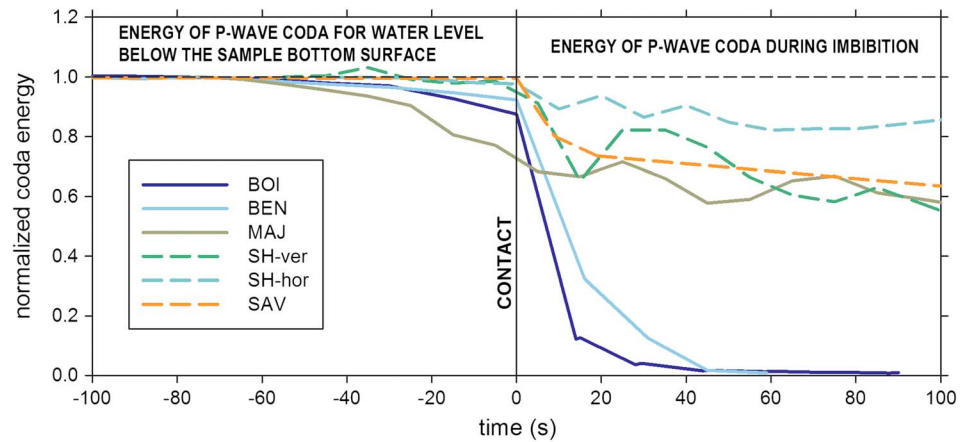


Figure B1. Energy of the *P* wave coda before ($t < 0$) and after ($t > 0$) water contacts the bottom end of the rock sample. The color coding is the same as in Figure 3.

To assess further this interpretation, a quantitative analysis of moisture diffusion length and time is carried out. The location of the water level in the tank is derived from the X-ray images and yields the free diffusion length L of water vapor in the air below the bottom end of the sample. Considering the first time step, the distance L is the largest (~ 10 mm), the diffusion time in air is $L^2/D_o = 3.5$ s which is smaller than the time lag between two consecutive images in Figure B2. Therefore, moisture diffusion is likely to impact the bottom end of the sample on a time scale compatible with our data sampling rate. On the other hand, the time of impact of moisture on seismic attributes recorded within the rock is controlled by the rock-dependent effective moisture diffusivity discussed in the main article. This is consistent with the early impact observed on samples belonging to the blue and green groups (high effective diffusivity) and lack of effect observed on samples belonging to the red group (low effective diffusivity). When the rock effective diffusivity is high, moisture measurably affects the wave attributes of the reflected waves: to our knowledge, this phenomenon has not been documented so far in the literature.

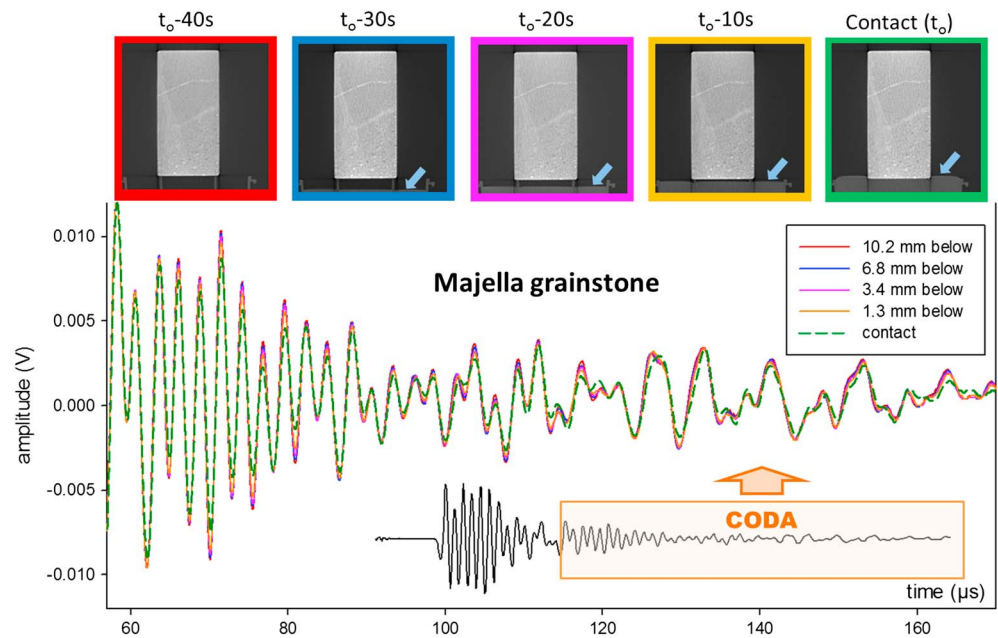


Figure B2. Evolution of the coda for Majella grainstone before the arrival of the water at the bottom of the sample. The color of each waveform corresponds to the background color of the CT-scan images. The inserted graph represents the full waveform from which the coda is extracted.

Acknowledgments

The very first experiments on Saint-Maximin limestone were conducted by Delphine Bertauld during her internship at CSIRO. We acknowledge financial support of the Onshore Gas Program through the Strategic Research Fund 2016–2017. Many thanks to Shane Kager, Stephen Firms, and David Nguyen for technical support. Some of the reservoir analogues tested here are available at Kocurek Industries (<http://www.kocurekindustries.com/>). The data set can be made available upon request. Many thanks to both reviewers and to the Associate Editor who helped in improving the manuscript.

References

- Avseth, P., T. Mukerji, and G. Mavko (2005), *Quantitative Seismic Interpretation: Applying Rock Physics Tools to Reduce Interpretation Risks*, 359 pp., Cambridge Univ. Press, Cambridge, U. K.
- Boving, T. B., and P. Grathwohl (2001), Tracer diffusion coefficients in sedimentary rocks: Correlation to porosity and hydraulic conductivity, *J. Contam. Hydrol.*, *53*(1), 85–100, doi:10.1016/S0169-7722(01)00138-3.
- Clark, V. A., B. R. Tittmann, and T. W. Spencer (1980), Effect of volatiles on attenuation (Q^{-1}) and velocity in sedimentary rocks, *J. Geophys. Res.*, *85*(B10), 5190–5198, doi:10.1029/JB085iB10p05190.
- Cussler, E. L. (1997), *Diffusion: Mass Transfer in Fluid Systems*, 2nd ed., 631 pp., Cambridge Univ. Press, Cambridge, U. K.
- Dautriat, J., J. Sarout, C. David, D. Bertauld, J. Sarout, and R. Macault (2016), Remote monitoring of the mechanical instability induced by fluid substitution and water weakening in the laboratory, *Phys. Earth Planet. Inter.*, *261*, 69–87, doi:10.1016/j.pepi.2016.06.011.
- David, C., Y. Gueguen, and G. Pampoukis (1990), Effective medium theory and network theory applied to the transport properties of rock, *J. Geophys. Res.*, *95*(B5), 6993, doi:10.1029/JB095iB05p06993.
- David, C., D. Bertauld, J. Dautriat, J. Sarout, B. Menéndez, and B. Nabawy (2015a), Detection of moving capillary front in porous rocks using X-ray and ultrasonic methods, *Front. Phys.*, *3*, 53, doi:10.3389/fphy.2015.00053.
- David, C., J. Dautriat, J. Sarout, C. Delle Piane, B. Menéndez, R. Macault, and D. Bertauld (2015b), Mechanical instability induced by water weakening in laboratory fluid injection tests, *J. Geophys. Res. Solid Earth*, *120*, 4171–4188, doi:10.1002/2015JB011894.
- David, C., C. Barnes, M. Desrues, L. Pimienta, J. Sarout, and J. Dautriat (2017), Ultrasonic monitoring of spontaneous imbibition experiments: Acoustic signature of fluid migration, *J. Geophys. Res. Solid Earth*, *122*, 4931–4947, doi:10.1002/2016JB013804.
- Digby, P. J. (1981), The effective elastic moduli of porous granular rocks, *J. Appl. Mech.*, *48*(4), 803, doi:10.1115/1.3157738.
- Doornhof, D., G. K. Tron, N. B. Nagel, P. D. Pattillo, and C. Sayers (2006), Compaction and subsidence, *Oilfield Rev.*, *18*(3), 50–68.
- Ghanbarian, B., A. G. Hunt, R. P. Ewing, and M. Sahimi (2013), Tortuosity in porous media: A critical review, *Soil Sci. Soc. Am. J.*, *77*(5), 1461, doi:10.2136/sssaj2012.0435.
- Hall, S. A. (2013), Characterization of fluid flow in a shear band in porous rock using neutron radiography, *Geophys. Res. Lett.*, *40*, 2613–2618, doi:10.1002/grl.50528.
- JafarGandomi, A., and A. Curtis (2011), Detectability of petrophysical properties of subsurface CO₂-saturated aquifer reservoirs using surface geophysical methods, *Leading Edge*, *30*(10), 1112–1121, doi:10.1190/1.3657069.
- Jaya, M., S. Shapiro, D. Bruhn, E. Huenges, and Ó. Flóvenz (2008), Temperature-dependent fluid substitution analysis of geothermal rocks at in-situ reservoir conditions, in *SEG Technical Program Expanded Abstracts 2008*, pp. 1774–1778, Society of Exploration Geophysicists, Las Vegas.
- Johnson, K. L., K. Kendall, and A. D. Roberts (1971), Surface energy and the contact of elastic solids, *Proc. R. Soc. London A*, *324*(1558), 301–313.
- Katz, A. J., and A. H. Thompson (1986), Quantitative prediction of permeability in porous rock, *Phys. Rev. B*, *34*(11), 8179–8181, doi:10.1103/PhysRevB.34.8179.
- Knight, R., and J. Dvorkin (1992), Seismic and electrical properties of sandstones at low saturations, *J. Geophys. Res.*, *97*(B12), 17,425, doi:10.1029/92JB01794.
- Le Ravalec, M., Y. Guéguen, and T. Chelidze (1996), Elastic wave velocities in partially saturated rocks: Saturation hysteresis, *J. Geophys. Res.*, *101*(B1), 837–844, doi:10.1029/95JB02879.
- Lopes, S., M. Lebedev, S. Lopes, and M. Lebedev (2012), Laboratory study of the influence of changing the injection rate on P-wave velocities and water saturation in a limestone, *ASEG Ext. Abstr.*, *2012*(1), 1, doi:10.1071/ASEG2012ab083.
- Lopes, S., M. Lebedev, and T. M. Müller (2013), Water imbibition into sandstones: Influence of flow rate on water distribution and acoustic response, in *Sandstone: Geochemistry, Uses and Environmental Impact*, pp. 37–64, Nova Sci., Hauppauge, New York.
- Lopes, S., M. Lebedev, T. M. Müller, M. B. Clennell, and B. Gurevich (2014), Forced imbibition into a limestone: Measuring P-wave velocity and water saturation dependence on injection rate, *Geophys. Prospect.*, *62*(5), 1126–1142, doi:10.1111/1365-2478.12111.
- Mavko, G., T. Mukerji, and J. Dvorkin (2009), *The Rock Physics Handbook: Tools for Seismic Analysis of Porous Media*, 2nd ed., 511 pp., Cambridge Univ. Press, Cambridge, U. K.
- Mees, F., R. Swennen, M. Van Geet, and P. Jacobs (2003), Applications of X-ray computed tomography in the geosciences, *Geol. Soc. London, Spec. Publ.*, *215*(1), 1–6, doi:10.1144/GSL.SP.2003.215.01.01.
- Murphy, W. F., K. W. Winkler, and R. L. Kleinberg (1984), Frame modulus reduction in sedimentary rocks: The effect of adsorption on grain contacts, *Geophys. Res. Lett.*, *11*(9), 805–808, doi:10.1029/GL011i009p00805.
- Novakowski, K. S., and R. W. Gillham (1988), Field investigations of the nature of water-table response to precipitation in shallow water-table environments, *J. Hydrol.*, *97*(1), 23–32, doi:10.1016/0022-1694(88)90063-7.
- Perkins, T. K., and O. C. Johnston (1963), A review of diffusion and dispersion in porous media, *Soc. Pet. Eng. J.*, *3*(1), 70–84, doi:10.2118/480-PA.
- Pimienta, L., J. Fortin, and Y. Gueguen (2014), Investigation of elastic weakening in limestone and sandstone samples from moisture adsorption, *Geophys. J. Int.*, *199*(1), 335–347, doi:10.1093/gji/ggu257.
- Qi, Q., T. M. Müller, B. Gurevich, S. Lopes, M. Lebedev, and E. Caspari (2014), Quantifying the effect of capillarity on attenuation and dispersion in patchy-saturated rocks, *Geophysics*, *79*(5), WB35–WB50, doi:10.1190/geo2013-0425.1.
- Rasolofosaon, P., and B. Zinszner (2004), Laboratory petroacoustics for seismic monitoring feasibility study, *Leading Edge*, *23*(3), 252–258, doi:10.1190/1.1690898.
- Rasolofosaon, P. N. J., and B. Zinszner (2012), Experimental verification of the petroelastic model in the laboratory—Fluid substitution and pressure effects, *Oil Gas Sci. Technol. – Rev. d'IFP Energies Nouv.*, *67*(2), 303–318, doi:10.2516/ogst/2011167.
- Shen, L., and Z. Chen (2007), Critical review of the impact of tortuosity on diffusion, *Chem. Eng. Sci.*, *62*(14), 3748–3755, doi:10.1016/j.ces.2007.03.041.
- Spetzler, J., and R. Snieder (2004), The Fresnel volume and transmitted waves, *Geophysics*, *69*(3), 653–663, doi:10.1190/1.1759451.
- van Brakel, J., and P. M. Heertjes (1974), Analysis of diffusion in macroporous media in terms of a porosity, a tortuosity and a constrictivity factor, *Int. J. Heat Mass Transfer*, *17*(9), 1093–1103, doi:10.1016/0017-9310(74)90190-2.
- van Den Abeele, K. E.-A., J. Carmeliet, P. A. Johnson, and B. Zinszner (2002), Influence of water saturation on the nonlinear elastic mesoscopic response in Earth materials and the implications to the mechanism of nonlinearity, *J. Geophys. Res.*, *107*(B6), 2121, doi:10.1029/2001JB000368.
- Stanchits, S., S. Mayr, S. Shapiro, and G. Dresen (2011), Fracturing of porous rock induced by fluid injection, *Tectonophysics*, *503*(1), 129–145, doi:10.1016/j.tecto.2010.09.022.

- Walsh, J. B., and W. F. Brace (1984), The effect of pressure on porosity and the transport properties of rock, *J. Geophys. Res.*, *89*(B11), 9425, doi:10.1029/JB089iB11p09425.
- Weissberg, H. L. (1963), Effective diffusion coefficient in porous media, *J. Appl. Phys.*, *34*(9), 2636–2639, doi:10.1063/1.1729783.
- Wulff, A., and S. Mjaaland (2002), Seismic monitoring of fluid fronts: An experimental study, *Geophysics*, *67*(1), 221–229, doi:10.1190/1.1451622.